CHIN. PHYS. LETT. Vol. 38, No. 5 (2021) 057402 **Express Letter**

Highly Robust Reentrant Superconductivity in CsV_3Sb_5 under Pressure

Xu Chen(陈旭)[1†], Xinhui Zhan(战鑫慧)[2†], Xiaojun Wang(王晓郡)[2], Jun Deng(邓俊)[1], Xiao-Bing Liu(刘晓兵)[2*], Xin Chen(陈欣)[2], Jian-Gang Guo(郭建刚)[1,3*], and Xiaolong Chen(陈小龙)[1,3*]

[1]*Beijing National Laboratory for Condensed Matter Physics, Institute of Physics, Chinese Academy of Sciences, Beijing 100190, China*

[2]*Laboratory of High Pressure Physics and Material Science (HPPMS), School of Physics and Physical Engineering, Qufu Normal University, Qufu 273100, China*

[3]*Songshan Lake Materials Laboratory, Dongguan 523808, China*

(Received 29 March 2021; accepted 14 April 2021; published online 20 April 2021)

We present the superconducting (SC) property and high-robustness of structural stability of kagome CsV_3Sb_5 under *in situ* high pressures. For the initial SC-I phase, its T_c is quickly enhanced from 3.5 K to 7.6 K and then totally suppressed at $P \sim 10$ GPa. With further increasing pressure, an SC-II phase emerges at $P \sim 15$ GPa and persists up to 100 GPa. The T_c rapidly increases to the maximal value of 5.2 K at $P = 53.6$ GPa and slowly decreases to 4.7 K at $P = 100$ GPa. A two-dome-like variation of T_c in CsV_3Sb_5 is concluded here. The Raman measurements demonstrate that weakening of E_{2g} mode and strengthening of E_{1g} mode occur without phase transition in the SC-II phase, which is supported by the results of phonon spectra calculations. Electronic structure calculations reveal that exertion of pressure may bridge the gap of topological surface nontrivial states near E_F, i.e., disappearance of Z_2 invariant. Meanwhile, the Fermi surface enlarges significantly, consistent with the increased carrier density. The findings here suggest that the change of electronic structure and strengthened electron-phonon coupling should be responsible for the pressure-induced reentrant SC.

DOI: 10.1088/0256-307X/38/5/057402

A kagome lattice, composed of atoms at the vertices of a two-dimensional network with the corner-sharing triangles, provides a fascinating playground for exploring the novel frustrated, correlated and topological electronic states of matters recently.[1−4] Due to the special geometry, the kagome lattice naturally possesses Dirac dispersion and nearly flat bands that promote topological and correlation effect.[5] Kagome systems are predicted to host too many exotic electronic states, such as spinless fermions,[6−8] Mott phase transition,[6,9,10] charge density waves (CDW),[6,11−13] and superconductivity (SC).[6,7,11,14] Up to date, exploring exotic properties, in particular, the interplay between multiple electronic orders in kagome lattices, have been of challenge.

Recently, a new family of quasi-2D kagome metals AV_3Sb_5 (A = K, Rb and Cs) have attracted considerable attention.[15] The vanadium sublattice of *P6/mmm* CsV_3Sb_5 is a structurally perfect kagome lattice. There are two distinct Sb sublattices. The sublattice formed by the Sb1 atom is a simple hexagonal net, centered on each kagome hexagon. All interatomic distances within the kagome layer are equal, as required by the high symmetry of the V1 (Wyckoff 3g) and Sb1 (Wyckoff 1b) sites. The Sb2 (Wyckoff 4h) sublattice creates graphite-like layers of Sb (antimonene) that encapsulate the kagome sheets. The Cs sublattice fills the space between the graphite-like sheets. The superconducting transition temperatures (T_c) are 0.93, 0.92, and 2.5 K for the three compounds, respectively.[16−18] In addition, in normal state they all manifest a proposed charge density wave transitions at 78, 103, and 94 K, respectively.[15,19,20] Interestingly, high-resolution scanning tunneling microscopy (STM) study reveals that such charge order displays a chiral anisotropy,[21−23] which leads to a giant anomalous Hall effect in the absence of resolvable magnetic order or local moments,[17,24−26] pointing to a precursor of unconventional SC.[21,27] Furthermore, the proximity-induced spin-triplet pairing and an edge supercurrent have been observed in Nb/KV_3Sb_5 devices.[28] More importantly, Z_2 nontrivial topological band structures, including multiple Dirac nodal points near the Fermi level (E_F) and possible topological surface states, were demonstrated by angle-resolved photoemission spectroscopy (ARPES) and density-functional theory (DFT) calculations.[15,16,18] Therefore, AV_3Sb_5 is regarded as a candidate to study the interplay among SC, electron correlation and nontrivial band topology.

Supported by the National Key Research and Development Program of China (Grant Nos. 2017YFA0304700, 2018YFE0202601, and 2016YFA0300600), the National Natural Science Foundation of China (Grant Nos. 51922105, 11804184, 11974208, and 51772322), the Chinese Academy of Sciences (Grant No. QYZDJ-SSW-SLH013), the Beijing Natural Science Foundation (Grant No. Z200005), and the Shandong Provincial Natural Science Foundation (Grant Nos. ZR2020YQ05, ZR2019MA054, and 2019KJJ020).

†Xu Chen and Xinhui Zhan contributed equally to this work.

*Corresponding authors. Email: xiaobing.phy@qfnu.edu.cn; jgguo@iphy.ac.cn; chenx29@iphy.ac.cn

© 2021 Chinese Physical Society and IOP Publishing Ltd

It is known that *in situ* pressure tuning is a 'clean' way to tune basic electronic and structural properties without changing the chemical composition, and eventually benefits for elucidating mechanisms of the puzzling state in new superconducting materials.[29−34] Very recently, Zhao *et al.* and Chen *et al.* reported that the T_c of CsV_3Sb_5 first increases to 7.5 K and quickly reduces under pressure, proving the competition between SC and possible CDW.[27,35] Then, Zhao *et al.* and Zhang *et al.* updated the data of relatively high pressure, and the reemergence of SC after 15 GPa was discovered.[27,36]

In this study, we performed the *in situ* high pressure transport measurements on the CsV_3Sb_5 sample as pressure is up to 100 GPa. Two superconducting domes in the temperature-pressure phase diagram are revealed. Interestingly, in pressure-induced superconducting state, the T_c and crystal structure are rather robust evidenced by the transport measurements, Raman spectra and phonon spectra calculations. Thus, varied electronic structure and possibly enhanced electron-phonon coupling play important roles in inducing reentrant SC.

Sample Preparation. Single crystals of CsV_3Sb_5 were grown from Cs (Alfa, 99.98%), V powder (Alfa, 99.9%) and Sb grains (Alfa, 99.999%) using the self-flux growth method similar to the previous reports.[15] Cs, V and Sb were weighted as the stoichiometric ratio in an argon-filled glove box (A small excess of Cs was used to compensate for volatility of the alkali metal). Then they were packed into Al_2O_3 crucible in order and sealed into an evacuated silica tube under partial argon atmosphere. The sealed quartz ampoule was heated to 1273 K and soaked there for 24 h. Then, it was cooled down to 823 K at 2 K/h. Finally, the ampoule was taken out from the box furnace and decanted with a centrifuge to separate CsV_3Sb_5 single crystals from the flux. The shinning CsV_3Sb_5 single crystals were obtained, see Fig. S1 (in the Supporting Information).

In Situ High-Pressure Measurements. High pressure resistivity of CsV_3Sb_5 single crystals was measured in a physical property measurement system (PPMS, Quantum Design) using a diamond anvil cell (DAC) at temperatures of 2–300 K. We used the van der Pauw method for electrical transport measurements on the CsV_3Sb_5 samples. Be–Cu cells were used for the resistance experiments. The cubic boron nitride (cBN) powders (200 and 300 nm in diameter) were employed as the pressure medium and the insulating material. The pressure was measured using the ruby fluorescence method at room temperature each time before and after the measurement. In addition, *in situ* Raman spectra under high pressure were taken (Horiba, Lab- RAM HR revolution) to characterize their structures.

Theoretical Calculations. We performed structural optimization and electronic property calculations within framework of the DFT + U by the Vienna *ab initio* simulation package (VASP) code.[37−40] The generalized-gradient approximation (GGA) is used for the exchange-correlation term within the Perdew–Burke–Ernzerhof (PBE) approach.[41−43] The additional Hubbard-like term is used to treat the on-site Coulomb interactions on the localized d-states of vanadium atoms. A plane wave energy cutoff of 350 eV and the Monkhorst–Pack k-meshes with a maximum spacing of $2\pi \times 0.15$ Å^{-1} were used to ensure that all the enthalpy calculations are well converged to better than 1 meV/atom. To examine the dynamical stability of the structure, we performed phonon calculations using the finite displacement method as implemented in the PHONOPY code.[44] The Brillouin zone was sampled with a $3 \times 3 \times 2$ supercell. Crystal orbital Hamilton population (COHP) analysis was performed using the LOBSTER package[45,46] in conjunction with VASP.

Results and Discussion. In the inset of Fig. 1(a), one can see that the temperature-dependent resistivity of CsV_3Sb_5 under ambient pressure, in which the kinks due to proposed charge density wave of 90 K and SC of 3.5 K coexist. The residual resistivity ratio value is about 25, indicating good quality of our sample. In a typical *in situ* high pressure measurement (run 1), two clear features emerge as shown in the main panel of Fig. 1(a). Firstly, the T_c^{onset} of SC-I phase increases to 7.6 K at 0.7 GPa and then decreases to below 2 K at 9.0 GPa, leading to a dome-like T_c. This pressure-dependent T_c is consistent with the recent reports.[27,35] The H-dependent resistivity at 1.5 GPa are plotted in Fig. 1(b). It is found that the H of 3.0 T can totally suppress the superconducting transition. The upper critical field $\mu_0 H_{c2}$, 4.2 T, is obtained based on the linear fitting. Another feature is that the magnitude of resistivity and the slops of the ρ–T curve continuously decrease. The former is due to the pressure-induced compact of crystal, and the latter may relate to the variation of electron-phonon coupling under pressure. In Fig. 1(c), we can find that the sample is normal metal without any signature of SC in the pressure range of 12.0–14.9 GPa. The total magnitude of resistivity and residual resistivity increases with P. As $P > 19.5$ GPa, a new superconducting phase appears. The T_c^{onset} of reentrant SC is 2.8 K, which slowly increases to T_c of ∼5.1 K at ∼57.1 GPa. It should be noted is that the SC phase survives after the pressure is released, indicating a reversible structure even the pressure is squeezed up to 57.1 GPa, see Fig. S2. In run 2, we further increase the pressure to 100 GPa. In Fig. 1(d), it is found that the second SC reenters as $P > 20$ GPa, exhibits peak T_c^{onset} of 5.2 K at 53.6 GPa and then gradually decreases. The T_c is rather robust against pressure. At 100 GPa, the T_c^{onset} is 4.7 K. We measured the H-dependent superconducting transition under $P = 53.6$ GPa, and plotted the

curves in Fig. 1(e). The SC is suppressed as $H > 2$ T. The calculated $\mu_0 H_{c2}(0)$ is about 3.5 T. We show the temperature-dependent $\mu_0 H_{c2}$ of CsV_3Sb_5 under selected pressure. The pressure dependence of $\mu_0 H_{c2}$ are plotted in Fig. 1(f) and Fig. S3, and the values are smaller than the Pauli limit of $1.84T_c$.

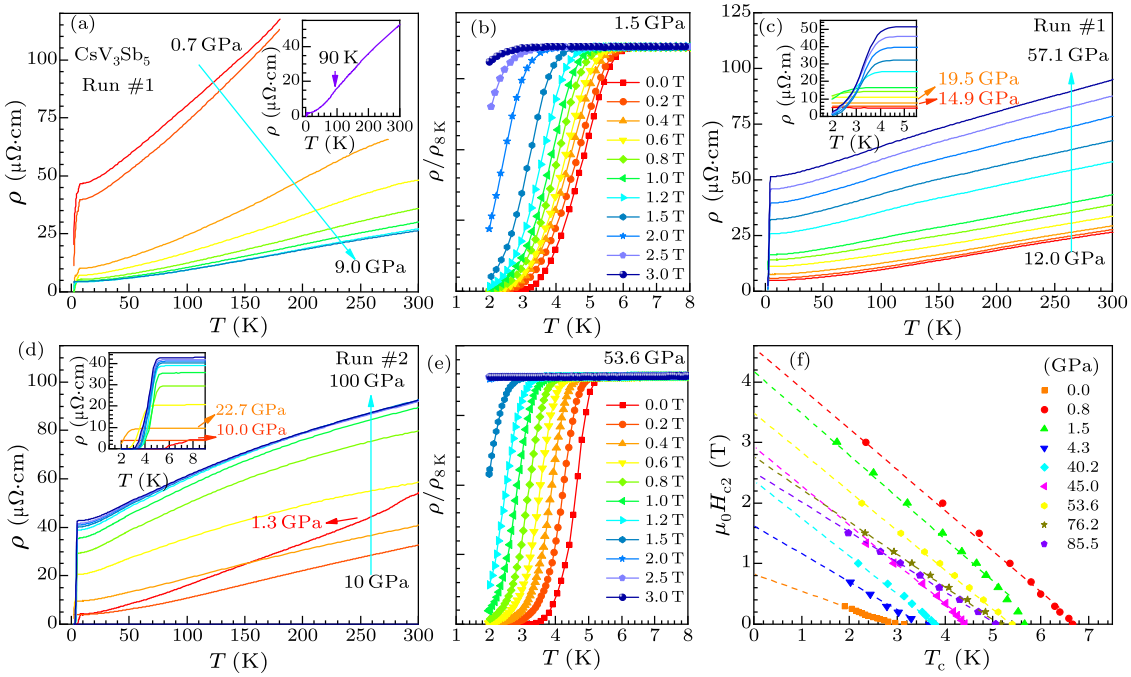

Fig. 1. Transport properties of CsV_3Sb_5 at various pressures. (a) The ρ–T curves in the temperature range 2–300 K for 0.7–9.0 GPa. The inset of (a) is the ρ–T curve for 0 GPa. (b) The ρ/ρ_{8K} around T_c under external magnetic field at 1.5 GPa. (c) The ρ–T curves in the temperature range 2–300 K for 12.0–57.1 GPa. The inset of (c) is the ρ–T curves in the temperature range 2–6 K. (d) The ρ–T curves in the temperature range 2–300 K for 1.3–100 GPa. The inset of (d) is the ρ–T curve in the temperature range 2–6 K. (e) Behavior of ρ/ρ_{8K} around T_c under external magnetic field at 53.6 GPa. (f) Temperature dependence of the upper critical field $\mu_0 H_{c2}$ at different pressures. The broken lines represent the linear fitting curves.

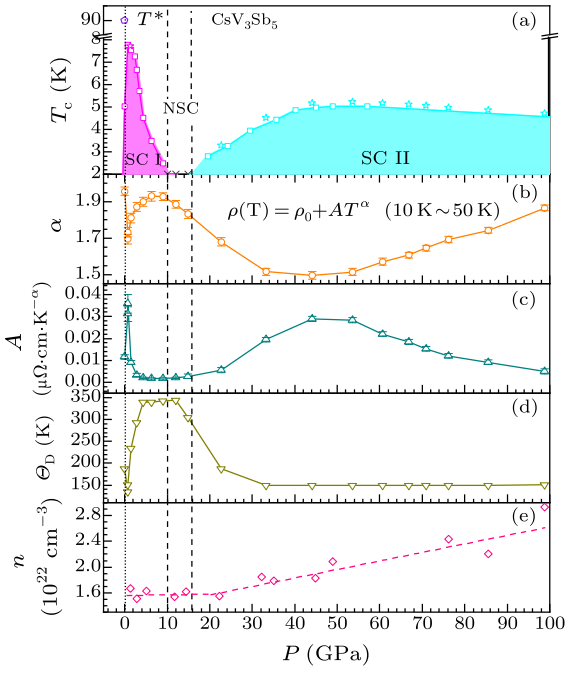

Fig. 2. Pressure dependence of (a) T_c and related physical parameters of CsV_3Sb_5: (b) index α, (c) prefactor A, (d) Debye temperature Θ_D, and (e) carrier density n.

The pressure-dependent T_c and related physical parameters are summarized in Fig. 2. There are two dome-like superconducting states under pressure as shown in Fig. 2(a). In the first SC range (SC-I), applying pressure rapidly enhances the T_c to ~7.6 K and then suppresses the T_c below 2 K as $P \sim 10$ GPa. In the second SC range (SC-Ⅱ), as $P > 15$ GPa, the T_c continuously increases to the highest T_c of 5.2 K, which is slightly lower than that in the SC-I region. The two SC ranges are separated by ~10 GPa. As previously reported, the highest T_c of reentrant SC is higher than that in SC-I phase such as FeSe-based superconductors. In $K_xFe_2Se_2$ and $(Li_{1-x}Fe_x)OHFe_{1-y}Se$ superconductors, the SC-I phases of 30 K and 41 K are rapidly suppressed at $P = 10$ GPa and 4 GPa, respectively. Then pressure-induced SC-Ⅱ phases emerge with the maximum T_c of 48.7 K and 50 K.[33,47,48] According to the transport property analysis, the suppression of the first SC phase is related to a possible quantum phase transition from Fermi liquid to non-Fermi liquid behavior.[49] In some superconductors such as KMo_3As_3, the T_c of the pressure-induced SC-Ⅱ phase is slightly lower than that of the initial SC-I phase.[50]

In the normal state, the pressure-dependent key transport parameters are plotted in Figs. 2(b)–2(f). We fit the $\rho(T)$ curve by the equation $\rho = \rho_0 + AT^{\alpha}$ from T_c to 50 K. Here ρ_0 is residual resistivity, and A is constant. The pressure-dependent index α is plotted in Fig. 2(b). In the SC-I, the α increases from 1.69 to 1.93, then it continuously decreases to 1.50 as the reentrant SC occurs. As the P goes through the optimal value, the α increases again to 1.87. Such behaviors imply that the electron-correlated states possibly transit from Fermi-liquid to non-Fermi-liquid state, and then back to Fermi-liquid state again.[51,52] For the A, in SC-I region, it quickly increases to the peak value at 0.7 GPa, and then lowers to the minimum as the T_c is totally suppressed, see Fig. 2(c). In the NSC and SC-Ⅱ regions, the A shows the peak value of $0.029\,\mu\Omega{\cdot}\mathrm{cm}{\cdot}\mathrm{K}^{-\alpha}$. On the other hand, in a pressurized sample, the ρ_0 generally decreases with increasing P, similar to the trend in the SC-I region. However, the enhancement of ρ_0 in higher P is unusual, which may be caused by disorder if there is no metal-insulator transition.

Based on the Bloch–Grüneisen model of scattering of electrons by longitudinal acoustic vibrations:[53]

$$\rho(T) = \rho_0 + B \times \frac{T^n}{\theta_D^{n-1}} \int_0^{\theta_D/T} \frac{z^n dz}{(e^z - 1)(1 - e^{-z})} - kT^3,$$

where ρ_0 is residual resistivity, the value of n is typically fixed at 3, k the coefficient of the cubic term, Θ_D the Debye temperature from the resistivity data, and B a prefactor depending on the material. We fitted the $\rho(T)$ data above T_c at each P, and obtained the Θ_D as shown in Fig. 2(d). It can be found that the Θ_D firstly rapidly increases to the maximal 344 K in the SC-I range, and then slowly decreases to a constant value of 150 K as entering the SC-Ⅱ range, implying reduction of average frequency of phonon vibration. In addition, we measure the pressure-dependent carrier density n as shown in Fig. 2(e), and find that it gradually increases from $1.6 \times 10^{22}\ \mathrm{cm}^{-3}$ to $2.9 \times 10^{22}\ \mathrm{cm}^{-3}$. The magnitude of n is consistent with the reported values in analogous compounds.[24,25]

It is instructive to check the structural stability at high pressure, thus we calculated phonon dispersions and projected phonon density of states at $P = 0$ GPa, 10 GPa, 20 GPa, 40 GPa, and 60 GPa, see Figs. S4 and S5. The optimized crystallographic parameters are summarized in Table S1. The phonon dispersions at $P = 0$ GPa exhibit large negative frequency at multiple directions in the Brillouin zone, indicating the structural instability. A 2×2 CDW ground state due to Peierls instability is proposed in the kagome lattice.[54] However, no imaginary frequencies are observed at higher pressure, suggesting that the dynamical stability enhances under pressure. Moreover, the contributions of phonon dispersions mainly come from the vibration of V and Sb atoms. The heavier Sb atoms dominate the low-frequency branches, while the relatively light V atoms contribute significantly to the high-frequency modes. Cs vibration has a smaller contribution over the whole frequency range due to the negligible chemical bonding with Sb atoms. More interestingly, it is found from Fig. S5 that the low-energy acoustic phonons soften around the M point with increasing pressure up to 40 GPa.

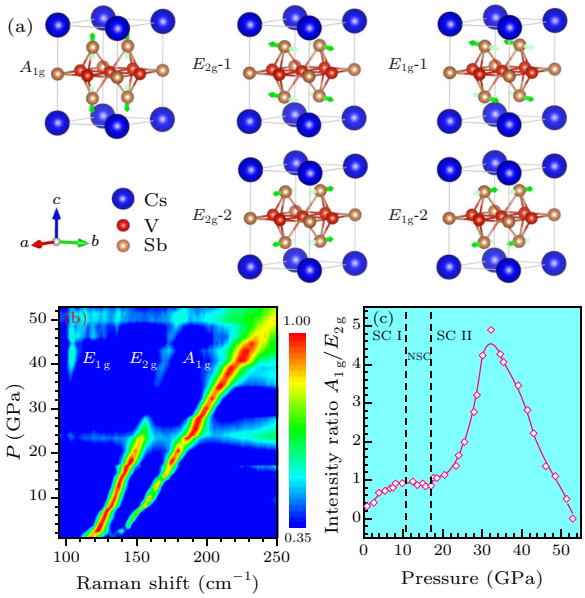

Fig. 3. (a) Three Raman-active modes of CsV_3Sb_5 as A_{1g}, E_{2g} and E_{1g}. (b) Pressure-induced Raman intensity and position change of CsV_3Sb_5 in the pressure range of 1–53 GPa. (c) Intensity ratio of A_{1g}/E_{2g} taken from (b).

On the other hand, according to the structural symmetry, three Raman-active models assigned as A_{1g}, E_{2g} and E_{1g} due to vibration of Sb are drawn in Fig. 3(a). The peak positions of three modes can be theoretically estimated from the phonon spectra at 10 GPa, 20 GPa, 40 GPa and 60 GPa. One can find that the three peaks are blue-shifted under applied pressure as shown in Fig. S6. We measured the pressure-dependent Raman spectra of CsV_3Sb_5 from 1 to 53 GPa and plotted them in Figs. 3(b), S7 and S8. At low P, two peaks of 119.5 cm^{-1} and 135.3 cm^{-1} are observed, which belong to E_{2g} and A_{1g} modes associated with longitudinal and transversal vibrations of Sb atoms. As $P > 20$ GPa, a small peak at ~100 cm^{-1} emerges, which is E_{1g} mode associated with in-plane relative vibration of upper Sb and lower Sb atoms. With increasing P, the peaks of E_{2g} and A_{1g} move to higher wave numbers like the observations in $MnBi_2Te_4$.[55] Simultaneously, the intensity of E_{2g} slowly decreases while that of A_{1g} increases. This anomalous change leads to the fact that the intensity ratio of A_{1g}/E_{2g} starts to increase as $P > 20$ GPa, then reaches the peak value at $P = 30$ GPa, see Fig. 3(c). At the same time, from the P-dependent Raman spectra in the right panel of Fig. S7, we can see that the E_{1g} mode emerges at 20.5 GPa. From the

above lattice dynamic information, we can deduce that the initial structure of CsV_3Sb_5 with space group of *P6/mmm* is very robust, and no structural transition happens as $P = 53$ GPa. Intuitively, the reentrant SC may relate to enhanced vibration of the low frequency E_{1g} and weakened vibration of the high frequency E_{2g}, which may partially strengthen electron-phonon coupling.

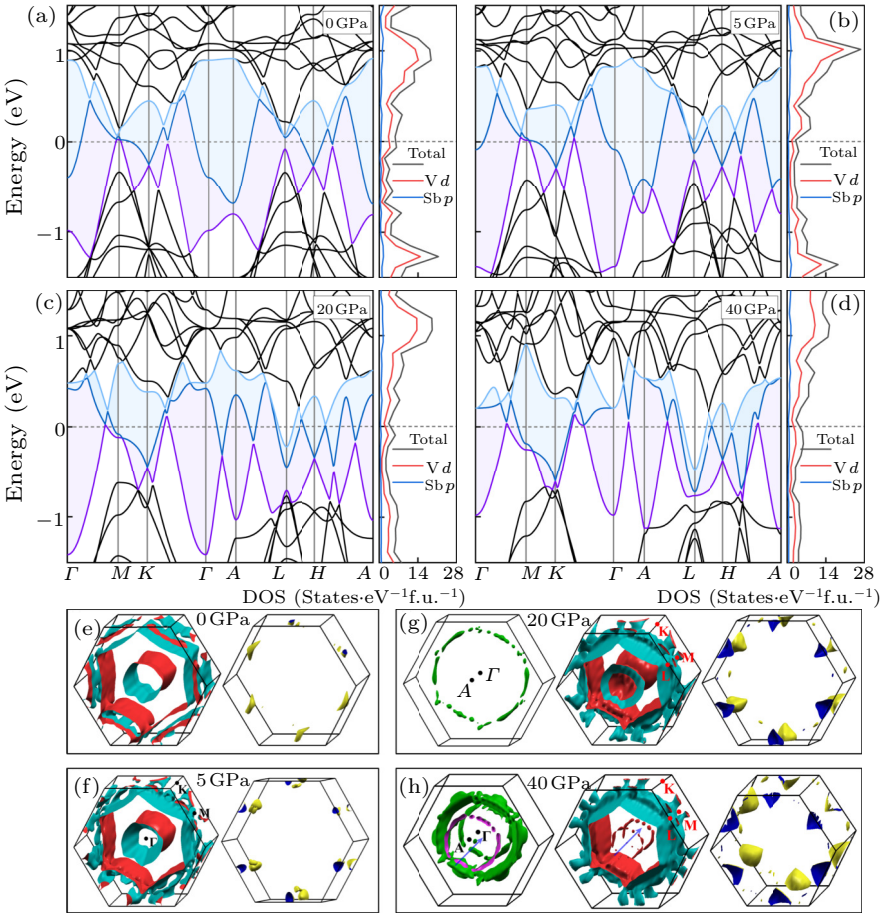

Fig. 4. Electronic band structures and partial density of states (PDOS) for CsV_3Sb_5 at (a) 0 GPa, (b) 5 GPa, (c) 20 GPa and (d) 40 GPa. Three bands crossing the E_F are plotted with different colors (light blue, blue and purple). The Fermi surface of each band crossing the Fermi energy at (e) 0 GPa, (f) 5 GPa, (g) 20 GPa and (h) 40 GPa. The blue arrows in Fig. 4(h) denote the nesting vector along Γ–A and L–M directions.

We calculated the electronic band structures at various pressures, as shown in Fig. 4. It can be seen that the electronic states of CsV_3Sb_5 near the E_F are mainly attributed by the V d and the Sb p orbitals. With the increase of pressure, the density of states (DOS) near E_F decreases from 5 to 3 states/eV per formula, see the right panels of Figs. 4(a)–4(d) and Fig. S9. Meanwhile, applying of pressure lifts the energy of middle band (blue color), closing the continuous direct gap in partial Brillouin zone. This implies that the Z_2 topological invariant may disappear at $P > 20$ GPa.[56,57] The Dirac-cone at the M point moves away from this high symmetry point at $P > 20$ GPa, and some more Dirac-like cones appear near Fermi surface at $P = 40$ GPa, see Figs. 4(c) and 4(d). In addition, the broadening of the band structure leads to more bands crossing through the E_F especially along Γ–A–L direction. From the pressure-dependent topology of Fermi surface [Figs. 4(e)–4(h)], it can be found that the scale of Fermi surface increases, consistent with the enhanced carrier density shown in Fig. 2(e). Interestingly, there are extra Fermi surface rings at $P = 20$ GPa and 40 GPa in Figs. 4(g) and 4(h), which supports the emergence of Lifshitz transition.[36] Strikingly, in Fig. 4(h), the *P6/mmm* structure exhibits Fermi surface nesting at $P = 40$ GPa along Γ–A and M–L directions, associated with highly dispersive bands in this directions as discussed above. Therefore, we suggest that the induced Fermi-surface nesting also favors the reemergence of SC-Ⅱ phase.

From Fig. S10(a), it is found that the lattice parameter c reduces rapidly in the low-pressure region and gradually changes slowly with the increasing pressure over 40 GPa. In contrast, the lattice parameter a does not change significantly, leading to the slow

decrease of interatomic distances within the kagome layer. Especially after 60 GPa, the bond length of V–Sb1 (V–V) exhibits a tendency to exceed that of V–Sb2 under pressure, see Fig. S10(b). In order to further investigate the bonding character of CsV_3Sb_5, we calculated projected crystal orbital Hamiltonian population (pCOHP) and plotted them in Fig. S11. It can evaluate the weighted population of wave functions on two atomic orbitals of a pair of selected atoms. It is noted that the occupied bonding states in CsV_3Sb_5 at 40 GPa move to deeper energy below the E_F, indicating higher stability of *P6/mmm* CsV_3Sb_5 at 40 GPa. Moreover, in Fig. S12, we use the integrated COHP (ICOHP) to quantitatively estimate the bonding strength. It is noted that the V–Sb1 covalent bonding in kagome net of vanadium is the strongest, and with increasing pressure, the V–Sb1 bond strengthens non-significantly as that of V–Sb2 and V–V bonds, suggesting the stable kagome layer upon compression as verified above.

In summary, we have investigated the SC, transport property and structural stability of CsV_3Sb_5 under high pressure up to 100 GPa. Initial SC phase-I is rapidly suppressed at $P \sim 10$ GPa, and then a second SC phase-Ⅱ emerges for $P > 15$ GPa. Interestingly, the SC-Ⅱ exhibits a dome-like T_c, in which the T_c quickly increases to peak T_c^{onset} of 5.2 K and then slowly decreases to 4.7 K at $P = 100$ GPa. Theoretical calculations and Raman measurements demonstrate that the initial crystal structure can persist in the whole pressure range. The reentrant SC should relate to variation of electronic structure and enhanced electron-phonon coupling due to partial phonon softening. The findings here suggest that the highly stable SC and structure in such kagome lattice deserve further investigation.

References

[1] Han T H, Helton J S, Chu S, Nocera D G, Rodriguez-Rivera J A, Broholm C and Lee Y S 2012 *Nature* **492** 406
[2] Sachdev S 1992 *Phys. Rev. B* **45** 12377
[3] Zhou Y, Kanoda K and Ng T K 2017 *Rev. Mod. Phys.* **89** 025003
[4] Bilitewski T and Moessner R 2018 *Phys. Rev. B* **98** 235109
[5] Mazin I I, Jeschke H O, Lechermann F, Lee H, Fink M, Thomale R and Valenti R 2014 *Nat. Commun.* **5** 4261
[6] Wang W S, Li Z Z, Xiang Y Y and Wang Q H 2013 *Phys. Rev. B* **87** 115135
[7] Ko W H, Lee P A and Wen X G 2009 *Phys. Rev. B* **79** 214502
[8] O'Brien A, Pollmann F and Fulde P 2010 *Phys. Rev. B* **81** 235115
[9] Isakov S V, Wessel S, Melko R G, Sengupta K and Kim Y B 2006 *Phys. Rev. Lett.* **97** 147202
[10] Yan S M, Huse D A and White S R 2011 *Science* **332** 1173
[11] Kiesel M L, Platt C and Thomale R 2013 *Phys. Rev. Lett.* **110** 126405
[12] Guo H M and Franz M 2009 *Phys. Rev. B* **80** 113102
[13] Rüegg A and Fiete G A 2011 *Phys. Rev. B* **83** 165118
[14] Yu S L and Li J X 2012 *Phys. Rev. B* **85** 144402
[15] Ortiz B R, Gomes L C, Morey J R, Winiarski M, Bordelon M, Mangum J S, Oswald I W H, Rodriguez-Rivera J A, Neilson J R, Wilson S D, Ertekin E, McQueen T M and Toberer E S 2019 *Phys. Rev. Mater.* **3** 094407
[16] Ortiz B R and Sarte P M 2020 arXiv:2012.09097 [cond-mat.supr-con]
[17] Yin Q W, Tu Z J, Gong C S, Fu Y, Yan S H and Lei H C 2021 *Chin. Phys. Lett.* **38** 037403
[18] Ortiz B R, Teicher S M L, Hu Y, Zuo J L, Sarte P M, Schueller E C, Abeykoon A M M, Krogstad M J, Rosenkranz S, Osborn R, Seshadri R, Balents L, He J F and Wilson S D 2020 *Phys. Rev. Lett.* **125** 247002
[19] Zhao H, Li H, Ortiz B R, Teicher S M L, Park T, Ye M, Wang Z, Balents L, Wilson S D and Zeljkovic I 2021 arXiv:2103.03118 [cond-mat.supr-con]
[20] Chen H, Yang H T, Hu B, Zhao Z, Yuan J, Xing Y Q, Qian G J, Huang Z H, Li G, Ye Y H, Yin Q W, Gong C S, Tu Z J, Lei H C, Ma S, Zhang H, Ni S L, Tan H X, Shen C M, Dong X L, Yan B H, Wang Z Q and Gao H J 2021 arXiv:2103.09188 [cond-mat.supr-con]
[21] Jiang Y X, Yin J X, Denner M M, Shumiya N, Ortiz B R, He J, Liu X, Zhang S S, Chang G, Belopolski I, Zhang Q, Hossain M S, Cochran T A, Multer D, Litskevich M, Cheng Z J, Yang X P, Guguchia Z, Xu G, Wang Z, Neupert T, Wilson S D and Hasan M Z 2020 arXiv:2012.15709 [cond-mat.supr-con]
[22] Li H X, Zhang T T, Pai Y Y, Marvinney C, Said A, Yilmaz T, Yin Q, Gong C, Tu Z, Vescovo E, Moore R G, Murakami S, Lei H C, Lee H N, Lawrie B and Miao H 2021 arXiv:2103.09769 [cond-mat.supr-con]
[23] Liang Z W, Hou X Y, Ma W R, Zhang F, Wu P, Zhang Z Y, Yu F H, Ying J J, Jiang K, Shan L, Wang Z Y and Chen X H 2021 arXiv:2103.04760 [cond-mat.supr-con]
[24] Yang S Y, Wang Y J, Ortiz B R *et al.* 2020 *Sci. Adv.* **6** eabb6003
[25] Yu F H, Wu T, Wang Z Y, Lei B, Zhuo W Z, Ying J J and Chen X H 2021 arXiv:2102.10987 [cond-mat.supr-con]
[26] Kenney E M, Ortiz B R, Wang C, Wilson S D and Graf M J 2021 *J. Phys.: Condens. Matter* (in press)
[27] Zhao C C, Wang L S, Xia W, Yin Q W, Ni J M, Huang Y Y, Tu C P, Tao Z C, Tu Z J, Gong C S, Lei H C, Guo Y F, Yang X F and Li S Y 2021 arXiv:2102.08356 [cond-mat.supr-con]
[28] Wang Y, Yang S, Sivakumar P K, Ortiz B R, Teicher S M L, Wu H, Srivastava A K, Garg C, Liu D, Parkin S S P, Toberer E S, McQueen T, Wilson S D and Ali M N 2020 arXiv:2012.05898 [cond-mat.supr-con]
[29] Wu M K, Ashburn J R, Torng C J, Hor P H, Meng R L, Gao L, Huang Z J, Wang Y Q and Chu C W 1987 *Phys. Rev. Lett.* **58** 908
[30] Eggert J H, Hu J Z, Mao H K, Beauvais L, Meng R L and Chu C W 1994 *Phys. Rev. B* **49** 15299
[31] Jia Y T, Gong C S, Liu Y X *et al.* 2020 *Chin. Phys. Lett.* **37** 097404
[32] Takahashi H, Igawa K, Arii K, Kamihara Y, Hirano M and Hosono H 2008 *Nature* **453** 376
[33] Sun L L, Chen X J, Guo J, Gao P W, Huang Q Z, Wang H D, Fang M H, Chen X L, Chen G F, Wu Q, Zhang C, Gu D C, Dong X L, Wang L, Yang K, Li A G, Dai X, Mao H K and Zhao Z X 2012 *Nature* **483** 67
[34] Liu Z Y, Dong Q X, Shan P F *et al.* 2020 *Chin. Phys. Lett.* **37** 047102
[35] Chen K Y, Wang N N, Yin Q W, Tu Z J, Gong C S, Sun J P, Lei H C, Uwatoko Y and Cheng J G 2021 arXiv:2102.09328 [cond-mat.supr-con]
[36] Zhang Z Y, Chen Z, Zhou Y, Yuan Y F, Wang S Y, Zhang L L, Zhu X D, Zhou Y H, Chen X L, Zhou J H and Yang Z R 2021 arXiv:2103.12507 [cond-mat.supr-con]
[37] Kohn W and Sham L J 1965 *Phys. Rev.* **140** A1133
[38] Lich H L 1989 *Phys. Rev. Lett.* **62** 1201
[39] Vladimir I, Anisimov J Z and Ole K 1991 *Phys. Rev. B* **44** 943
[40] Kresse G and Furthmüller J 1996 *Comput. Mater. Sci.* **6**

15
[41] Kresse G, Furthmüller J and Hafner J 1994 *Phys. Rev. B* **50** 13181
[42] Payne M C, Teter M P, Allan D C, Arias T and Joannopoulos A J 1992 *Rev. Mod. Phys.* **64** 1045
[43] Perdew J P, Burke K and Ernzerhof M 1996 *Phys. Rev. Lett.* **77** 3865
[44] Parlinski K, Li Z Q and Kawazoe Y 1997 *Phys. Rev. Lett.* **78** 4063
[45] Deringer V L, Tchougréeff A L and Dronskowski R 2011 *J. Phys. Chem. A* **115** 5461
[46] Maintz S, Deringer V L, Tchougreeff A L and Dronskowski R 2016 *J. Comput. Chem.* **7** 1030
[47] Sun J P, Shahi P, Zhou H X, Huang Y L, Chen K Y, Wang B S, Ni S L, Li N N, Zhang K, Yang W G, Uwatoko Y, Xing G, Sun J, Singh D J, Jin K, Zhou F, Zhang G M, Dong X L, Zhao Z X and Cheng J G 2018 *Nat. Commun.* **9** 380
[48] Shahi P, Sun J P, Wang S H, Jiao Y Y, Chen K Y, Sun S S, Lei H C, Uwatoko Y, Wang B S and Cheng J G 2018 *Phys. Rev. B* **97** 020508(R)
[49] Guo J, Chen X J, Dai J H, Zhang C, Guo J G, Chen X L, Wu Q, Gu D C, Gao P W, Yang L H, Yang K, Dai X, Mao H K, Sun L L and Zhao Z X 2012 *Phys. Rev. Lett.* **108** 197001
[50] Huang C, Guo J, Zhao K, Cui F, Qin S S, Mu Q G, Zhou Y Z, Cai S, Yang C L, Long S J, Yang K, Li A G, Wu Q, Ren Z A, Hu J P and Sun L L 2021 *Phys. Rev. Mater.* **5** L021801
[51] Nakatsuji S, Kuga K, Machida Y, Tayama T, Sakakibara T, Karaki Y, Ishimoto H, Yonezawa S, Maeno Y, Pearson E, Lonzarich G G, Balicas L, Lee H and Fisk Z 2008 *Nat. Phys.* **4** 603
[52] Luo Y, Pourovskii L, Rowley S E, Li Y, Feng C, Georges A, Dai J, Cao G, Xu Z, Si Q and Ong N P 2014 *Nat. Mater.* **13** 777
[53] Amon A, Svanidze E, Cardoso-Gil R, Wilson M N, Rosner H, Bobnar M, Schnelle W, Lynn J W, Gumeniuk R, Hennig C, Luke G M, Borrmann H, Leithe-Jasper A and Grin Y 2018 *Phys. Rev. B* **97** 014501
[54] Tan H, Liu Y Z, Wang Z Q and Yan B H 2021 arXiv:2103.06325 [cond-mat.supr-con]
[55] Pei C Y, Xia Y Y Y, Wu J Z *et al.* 2020 *Chin. Phys. Lett.* **37** 066401
[56] Schoop L M, Xie L S, Chen R, Gibson Q D, Lapidus S H, Kimchi I, Hirschberger M, Haldolaarachchige N, Ali M N, Belvin C A, Liang T, Neaton J B, Ong N P, Vishwanath A and Cava R J 2015 *Phys. Rev. B* **91** 214517
[57] Nayak J, Wu S C, Kumar N, Shekhar C, Singh S, Fink J, Rienks E E, Fecher G H, Parkin S S, Yan B H and Felser C 2017 *Nat. Commun.* **8** 13942

Supporting Information for "Highly-Robust Reentrant Superconductivity in CsV_3Sb_5 under Pressure"

Xu Chen(陈旭)[1]†, Xinhui Zhan(战鑫慧)[2]†, Xiaojun Wang(王晓郡)[2], Jun Deng(邓俊)[1], Xiao-Bing Liu(刘晓兵)[2*], Xin Chen(陈欣)[2], Jian-Gang Guo(郭建刚)[1,3*], and Xiaolong Chen(陈小龙)[1,3*]

[1]*Beijing National Laboratory for Condensed Matter Physics, Institute of Physics, Chinese Academy of Sciences, Beijing 100190, P. R. China*

[2]*Laboratory of High Pressure Physics and Material Science (HPPMS), School of Physics and Physical Engineering, Qufu Normal University, Qufu 273100, P. R. China*

[3]*Songshan Lake Materials Laboratory, Dongguan, Guangdong 523808, P. R. China*

†These authors contributed equally to this work.

*Corresponding authors.

Email: xiaobing.phy@qfnu.edu.cn; jgguo@iphy.ac.cn; chenx29@iphy.ac.cn

Table S1. Change of crystallographic parameters for CsV_3Sb_5 with respect to pressure in the range of 0-100 GPa.

Phase	Pressure (GPa)	Lattice parameters (Å, °)	Wuckoff position (fractional)			
			Atoms	x	y	z
P6/mmm	0	a = b = 5.49220 c = 9.88870 α = γ = 90.00 β = 120.00	Cs(1a)	0.0000	0.0000	0.0000
			V(3g)	0.5000	0.5000	0.5000
			Sb(1b)	0.0000	0.0000	0.5000
			Sb(4h)	0.6667	0.3333	0.7292
P6/mmm	5	a = b = 5.42020 c = 8.58070 α = γ = 90.00 β = 120.00	Cs(1a)	0.0000	0.0000	0.0000
			V(3g)	0.5000	0.5000	0.5000
			Sb(1b)	0.0000	0.0000	0.5000
			Sb(4h)	0.6667	0.3333	0.7612
P6/mmm	10	a = b = 5.3598 c = 8.11750 α = γ = 90.00 β = 120.00	Cs(1a)	0.0000	0.0000	0.0000
			V(3g)	0.5000	0.5000	0.5000
			Sb(1b)	0.0000	0.0000	0.5000
			Sb(4h)	0.6667	0.3333	0.7734
P6/mmm	20	a = b = 5.25530 c = 7.68210 α = γ = 90.00 β = 120.00	Cs(1a)	0.0000	0.0000	0.0000
			V(3g)	0.5000	0.5000	0.5000
			Sb(1b)	0.0000	0.0000	0.5000
			Sb(4h)	0.6667	0.3333	0.7840
P6/mmm	40	a = b = 5.10680 c = 7.19870 α = γ = 90.00 β = 120.00	Cs(1a)	0.0000	0.0000	0.0000
			V(3g)	0.5000	0.5000	0.5000
			Sb(1b)	0.0000	0.0000	0.5000
			Sb(4h)	0.6667	0.3333	0.7940
P6/mmm	60	a = b = 5.01490 c = 6.84900 α = γ = 90.00 β = 120.00	Cs(1a)	0.0000	0.0000	0.0000
			V(3g)	0.5000	0.5000	0.5000
			Sb(1b)	0.0000	0.0000	0.5000
			Sb(4h)	0.6667	0.3333	0.8000
P6/mmm	100	a = b = 4.85330 c = 6.52460 α = γ = 90.00 β = 120.00	Cs(1a)	0.0000	0.0000	0.0000
			V(3g)	0.5000	0.5000	0.5000
			Sb(1b)	0.0000	0.0000	0.5000
			Sb(4h)	0.6667	0.3333	0.8041

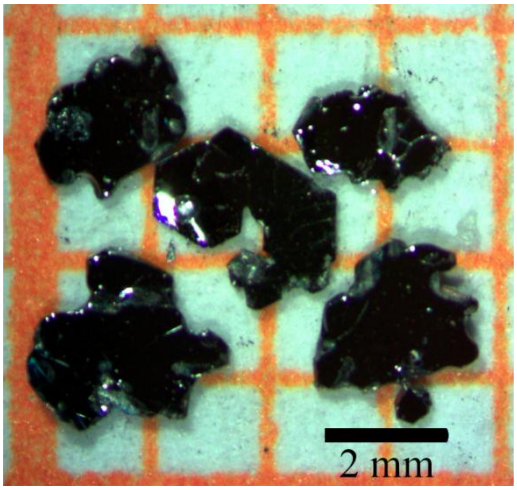

Figure S1. Optical photograph of CsV_3Sb_5 single crystals.

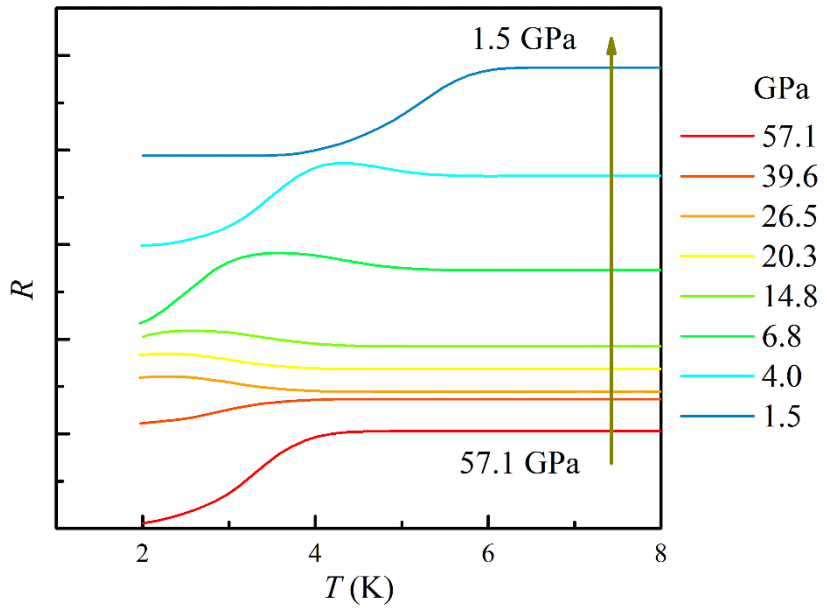

Figure S2. Temperature-dependent resistance of CsV_3Sb_5 at various pressures of 57.1-1.5 GPa,

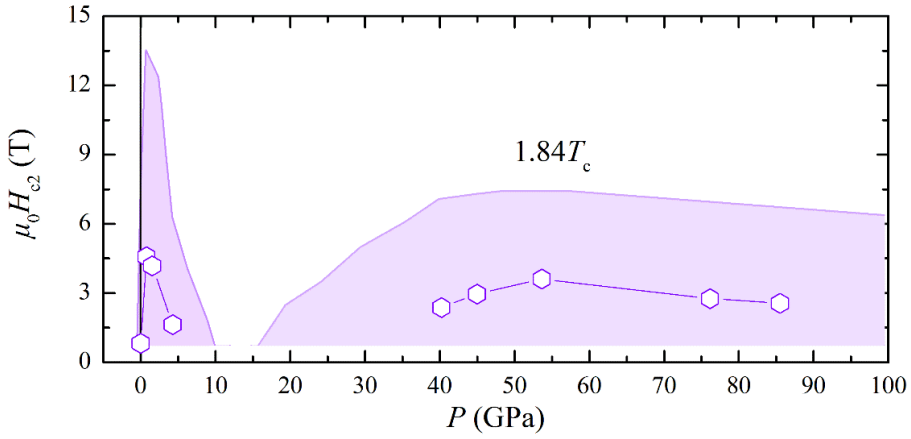

Figure S3. Pressure dependences of the upper critical field $\mu_0 H_{c2}(0)$ obtained from the linear fitting.

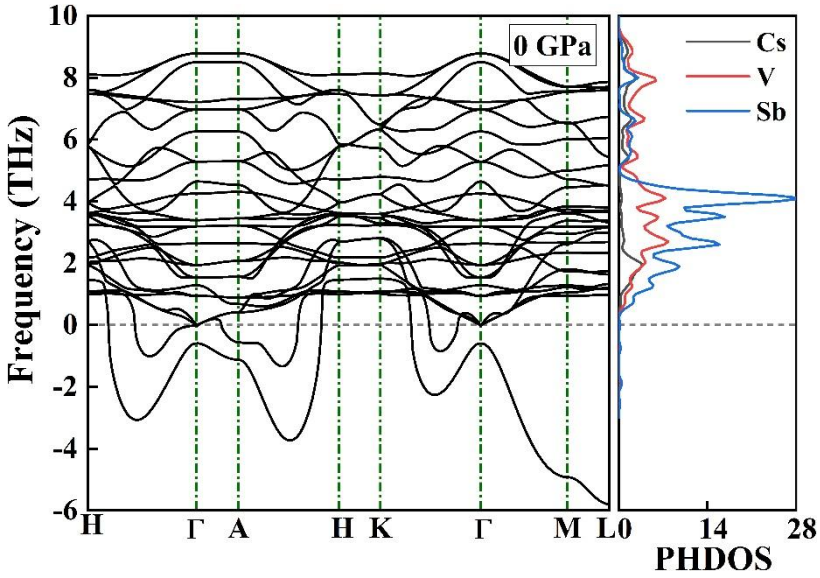

Figure S4. Calculated phonon dispersions and phonon density of states (PHDOS) of CsV_3Sb_5 at 0 GPa.

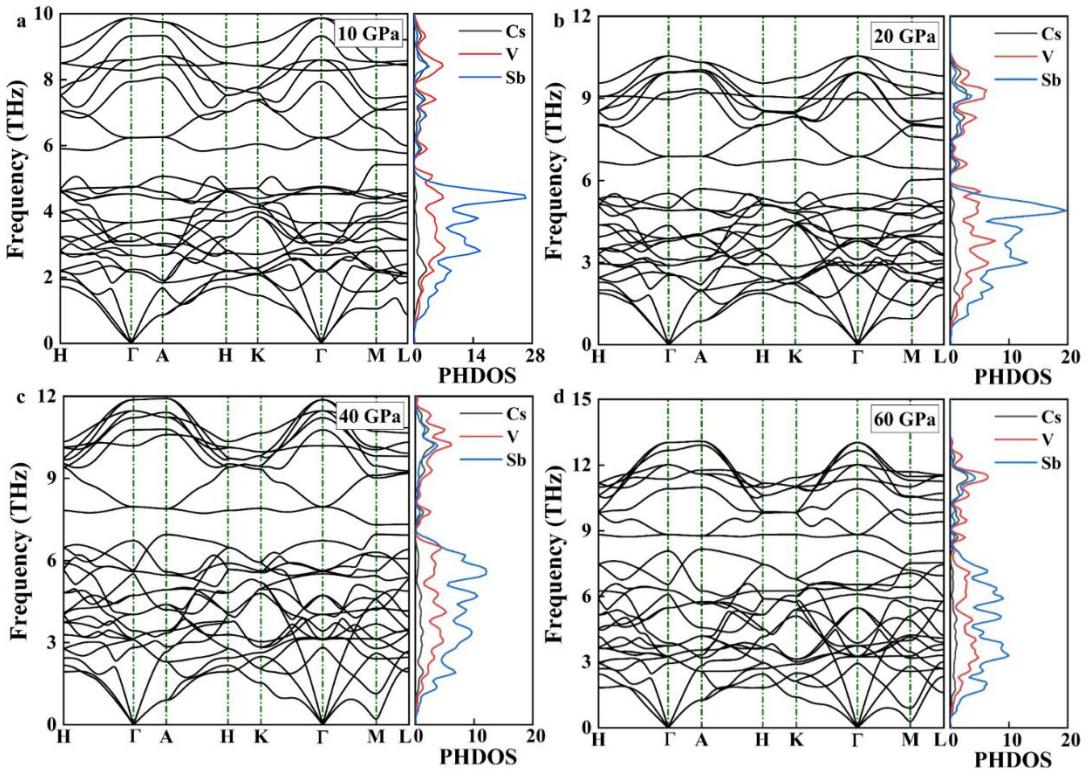

Figure S5. Calculated phonon dispersions and phonon density of states (PHDOS) of CsV_3Sb_5 at (a) 10 GPa, (b) 20 GPa, (c) 40 GPa, and (d) 60 GPa, respectively.

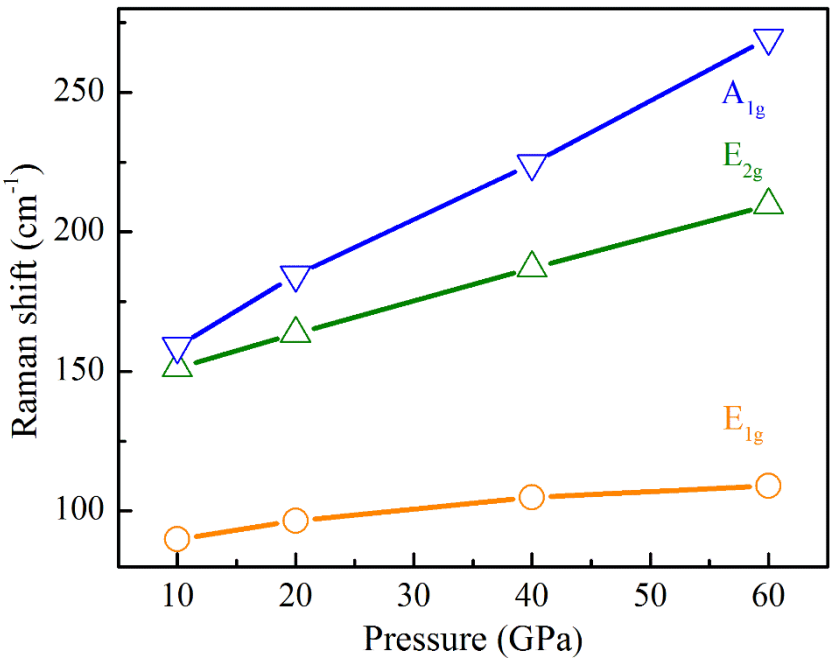

Figure S6. Pressure versus Raman frequency of CsV_3Sb_5 from phonon dispersions at 10 GPa, 20 GPa, 40 GPa and 60 GPa, respectively.

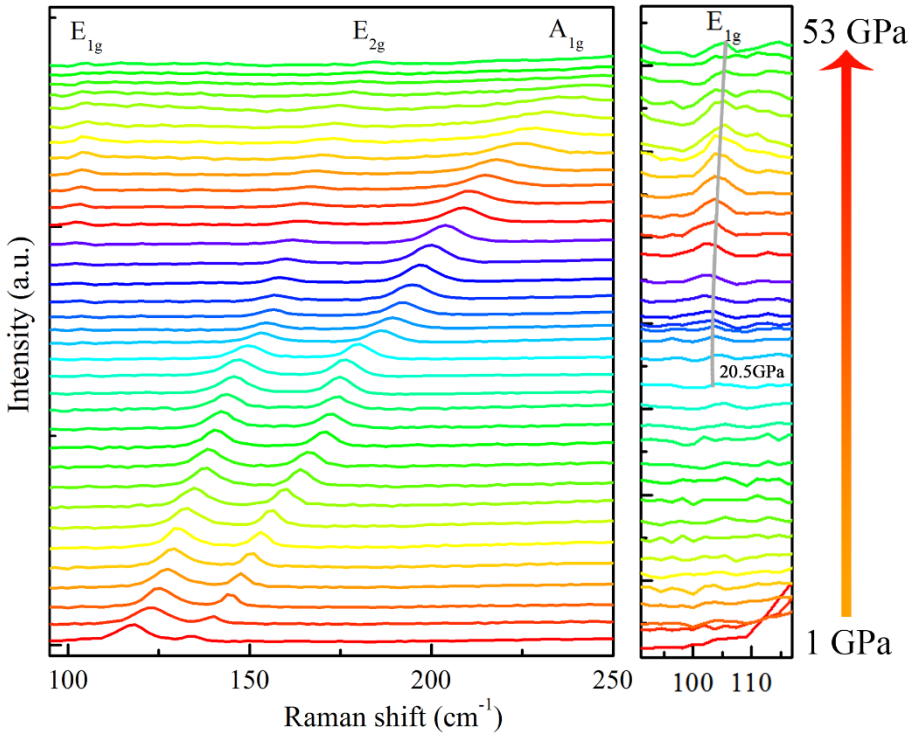

Figure S7. Pressure-induced Raman changes of CsV_3Sb_5 in the range of 1-53 GPa.

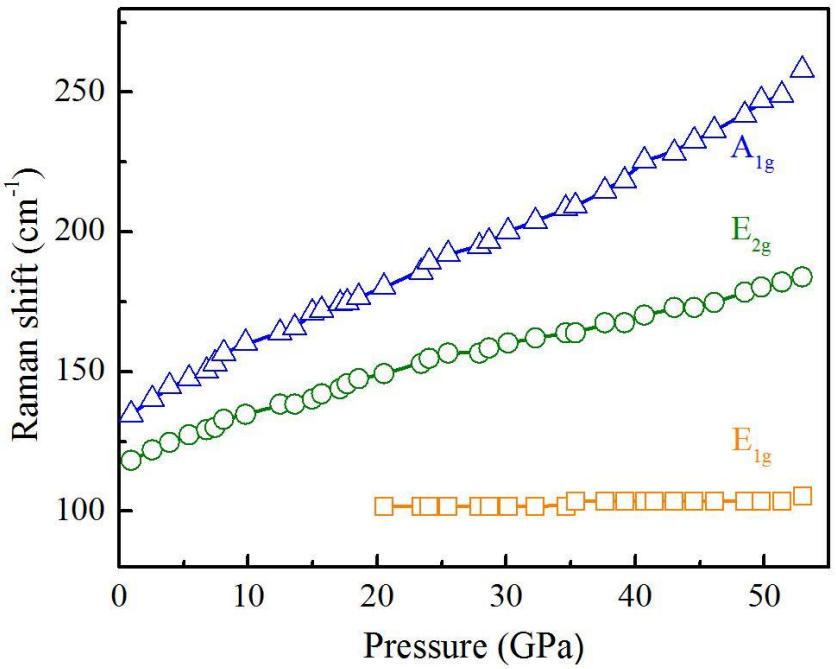

Figure S8. Pressure versus Raman frequency of CsV_3Sb_5 in the range of 1-53 GPa.

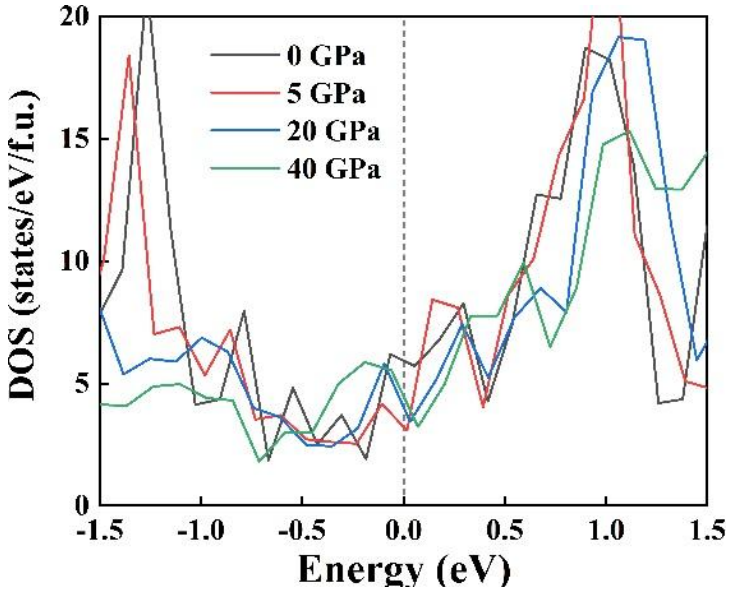

Figure S9. Calculated total density of states (DOS) for CsV_3Sb_5 at selected pressures.

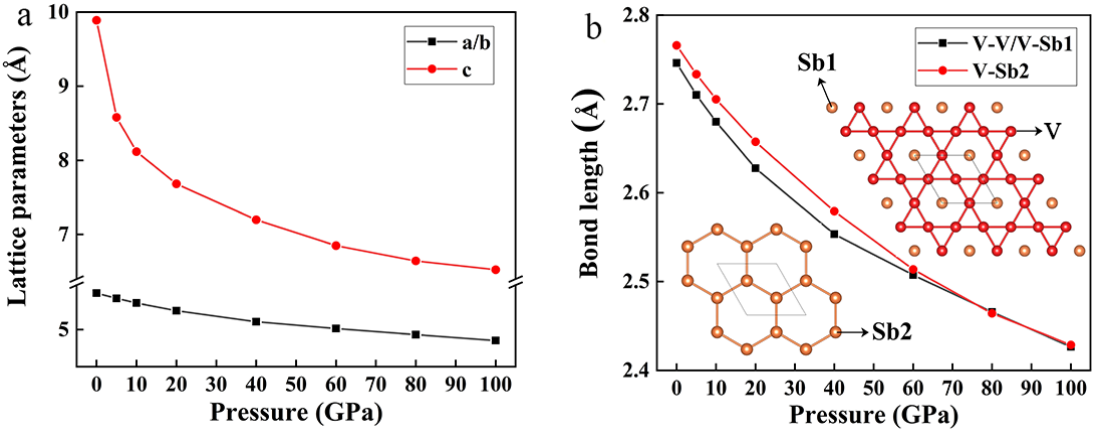

Figure S10. The change of lattice parameters (a) and bond lengths (b) with respect to pressure in the range of 0-100 GPa.

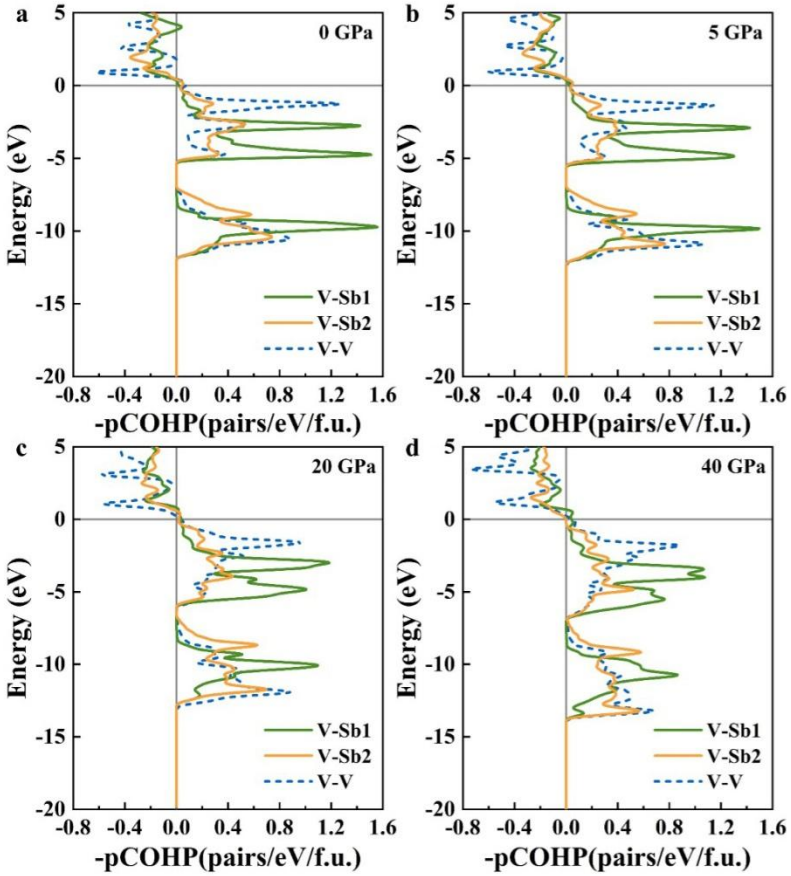

Figure S11. Projected crystal orbital Hamiltonian Population (-pCOHP) of CsV_3Sb_5 at (a) 0 GPa, (b) 5 GPa, (c) 20 GPa and (d) 40 GPa, respectively. The values of -pCOHP >0 signify bonding states and the values of -pCOHP <0 signify antibonding states. The Fermi level is set to zero.

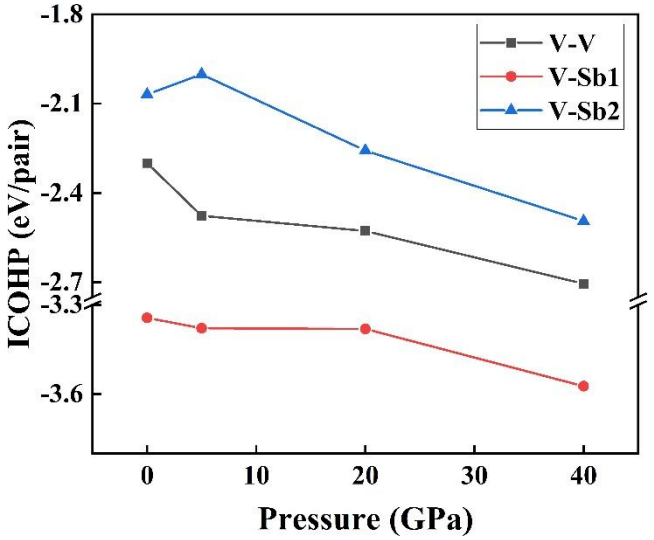

Figure S12. The integrated COHP (ICOHP) for V-V, V-Sb1 and V-Sb2 bonds of CsV_3Sb_5 at the range from 0 to 40 GPa.